

shamo: A tool for electromagnetic modelling, simulation and sensitivity analysis of the head

Martin Grignard ^{*}, Christophe Geuzaine [†], Christophe Phillips [‡]

Submitted on March 12, 2021

Abstract

Accurate electromagnetic modelling of the head of a subject is of main interest in the fields of source reconstruction and brain stimulation. Those processes rely heavily on the quality of the model and, even though the geometry of the tissues can be extracted from magnetic resonance images (MRI) or computed tomography (CT), their physical properties such as the electrical conductivity are hard to measure with non intrusive techniques. In this paper, we propose a tool to assess the uncertainty in the model parameters as well as compute a parametric electroencephalography (EEG) forward solution and current distribution for transcranial direct current stimulation (tDCS).

1 Introduction

Accurate electromagnetic modelling of the head is of main interest for source reconstruction techniques (EEG/MEG) and brain stimulation (tDCS/tMS). Such modelling must capture both the spatial distribution of the tissues and their physical properties, such as their electrical conductivity. The former can be extracted from different imaging techniques like magnetic resonance imaging (MRI) and computed tomography (CT) but the latter is very difficult to measure in vivo on a subject basis, even if some properties can be derived from specific MRI sequences [1].

Researchers thus have to rely on values of physical parameters reported in the literature, which can lead to erroneous electric field and potential estimations [2,3]. Indeed, inaccuracies on the physical parameters directly result in errors in the forward models, and thus in the reconstructed sources localisation or current flow. Several studies have been conducted on the sensitivity of the source reconstruction process to the electrical conductivity of the biological tissues [2–4]. Moreover, different models for the skull have been proposed [5,6] and the same goes for the anisotropy of white matter [7,8].

While those papers provide general hints about the sensitivity of the electromagnetic simulation to some input parameters, they remain sparse and are generally not performed on a subject basis. The present work introduces an open source package called *shamo* [9] which is dedicated to stochastic electromagnetic modelling of the head and sensitivity analysis of the results. The information made available by such a tool could help understand the

variability in studies results by giving a subject specific sensitivity index and thus improving the understanding of the effects of interest.

To highlight the mechanisms involved in the pipeline and demonstrate its usability and flexibility on actual cases, we apply it to the EEG forward problem and to trans-cranial direct current stimulation (tDCS) simulation. Both analysis are performed on a realistic finite element model (FEM) derived from the MIDA model [10]. To evaluate the impact of different geometries for the skull, we build three different models, going from a single isotropic compartment to a three layers skull with different electrical conductivities for the inner and outer tables.

The sensitivity is then assessed through the computation of Sobol indices. The random input parameters considered are the values for the electrical conductivity of the tissues. To model their probability density functions, we use the truncated normal distribution published in the recent review from McCann et al. [11] and an additional uniform distribution. In the process, we compute surrogate models that, for the EEG forward problem, results in a parametric leadfield matrix that can be used to generate new forward models for any set of electrical conductivity.

2 Materials and methods

2.1 Finite element model generation

In order to simulate the current flow inside the brain, a mathematical model is required. It must assess for both the geometry of the tissues and their properties. In this section, we focus on the geometrical aspect of such models.

Several methods to construct such models have been proposed [12] going from the multi-shells sphere to a fully fledged finite element model (FEM). In *shamo*, we consider the FEM approach with a similar toolset as [13]. This technique is able to capture complex shapes and

^{*}M. Grignard is with the GIGA CRC In-Vivo Imaging, University of Liège, Liège, Belgium (e-mail: mar.grignard@uliege.be)

[†]C. Geuzaine is with the Department of Electrical Engineering and Computer Science, University of Liège, Liège, Belgium (e-mail: cgeuzaine@uliege.be)

[‡]C. Phillips is with the GIGA CRC In-Vivo Imaging, University of Liège, Liège, Belgium (e-mail: c.phillips@uliege.be)

anisotropy can be incorporated in the form of a finite element field.

Usually, a key step in the generation of a realistic FEM of a head is the computation of the surfaces interfacing different tissue types. To avoid this complex process, we propose a pipeline where this step is eschewed and the mesh is produced directly from a segmented volume, i.e. where voxels are labelled as being of one tissue class. This allows us to work with more intricate structures and even to model less typical heads with prosthesis or deformities.

For this work, we start from the multimodal imaging-based detailed anatomical model of the human head and neck (MIDA) [10]. This model includes 116 structures stored in a $350 \times 480 \times 480$ matrix of $0.5 \text{ mm} \times 0.5 \text{ mm} \times 0.5 \text{ mm}$ voxels.

We consider three geometries based on the tissues considered for the models (see Table 1), specifically how the skull is modelled. In models 1, it is represented as a single isotropic tissue, for models 2, the upper part of the skull is separated into spongia and compacta. The latter is further divided into outer and inner tables for the models 3. Note though that the lower part of the skull is the same for all the models and is modelled as an homogeneous tissue class.

To obtain the corresponding segmented images, we merge the tissues of the MIDA model to keep only the main tissues (white matter, gray matter, cerebrospinal fluid, scalp and the different parts of the skull). The resulting models are illustrated in Figure 1.

Since we want to compare the outputs of the different models, we generate a tetrahedral mesh using CGAL [14] for the labelled voxels of model 3 which is the most complex one. The resulting mesh then serves as a base for the other models since we only have to merge the tissues to simplify the model 1 and 2. The merging step is performed with *Gmsh* [15]. This software is also used to annotate the mesh by specifying the names of the tissues and adding the electrodes on the scalp.

The output meshes all contain 1.355×10^6 tetrahedra and the 63 electrodes of the international 10-10 system [16] including the fiducial markers for the nose, the left and right ears and theinion. The latter is considered as the reference for the rest of this work.

2.2 Electromagnetic modelling

Since capacitive effects can be neglected in the brain tissues [17], electromagnetic fields at a time t only depend on the active sources at this time. Those conditions are referred to as quasi-static conditions. In such conditions, Maxwell's equations reduce to a generalized Poisson equation [12,18] which provides a relationship between the electric potential in any point of a volume conductor and the current sources.

We first define the current density \mathbf{j} (Am^{-2}) and the source volume current density ρ_s (Am^{-3}) [19]. They are linked together by the expression

$$\nabla \cdot \mathbf{j} = \rho_s. \quad (1)$$

The current density \mathbf{j} is linearly related to the electric

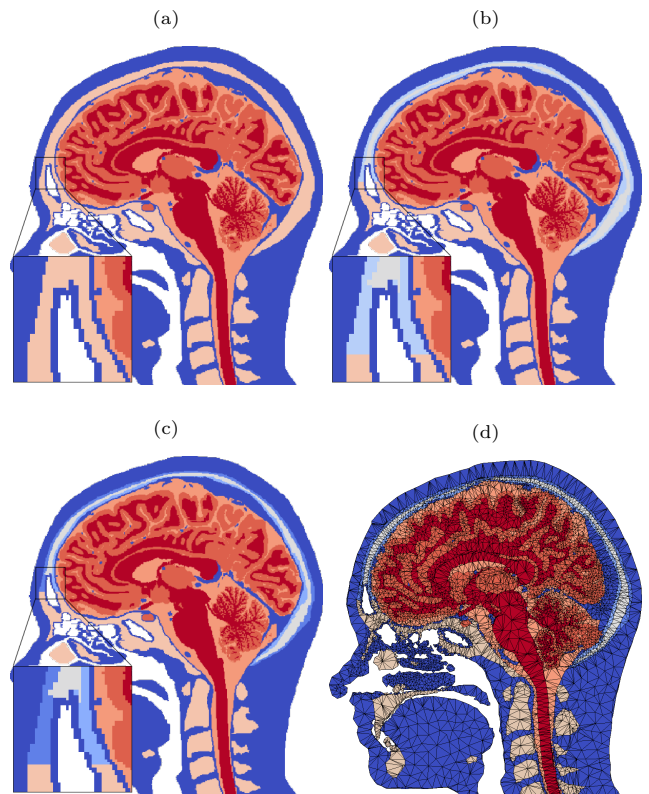


Fig. 1: Sagittal cuts of (a) the segmented images for models 1, (b) for models 2, (c) for models 3 and (d) the mesh corresponding to model 3.

field e (Vm^{-1}) through Ohm's law

$$\mathbf{j} = \sigma e \quad (2)$$

where σ can be a tensor field. In the present work, even though the anisotropy of the white matter has been shown to influence source reconstruction [4, 20] and the pipeline allows for anisotropic tissues, σ is considered isotropic due to the missing diffusion weighted images (DWI) in the MIDA model.

The quasi-static conditions described above allow us to write the relationship between the electric field and the electric potential field v (V) as

$$\mathbf{e} = -\nabla v. \quad (3)$$

Combining Equations (1), (2) and (3) leads to the generalized Poisson equation:

$$\nabla \cdot (\sigma \nabla(v)) = -\rho_s. \quad (4)$$

A homogeneous Neumann boundary condition is set on the interface between the conductor volume and the air and a Dirichlet condition is added to set the reference electrode. We use *GetDP* [21] as a solver for the finite element model described in section 2.1.

2.3 Tissues electrical conductivity

As shown in Equation (4), the electrical conductivity plays a major role in the computation of the electric potential

and the other related fields. Unfortunately, determining the exact electrical conductivity σ (Sm^{-1}) of the biological tissues in a non-intrusive manner is an open issue and many methods have been developed to measure it either in-vitro, ex-vivo or even in-vivo but struggle to provide an accurate and reliable value. In [11], McCann et al. reviewed the values acquired with different techniques and under specific conditions and derived an underlying probability distribution in the form of a truncated normal distribution for the main tissues composing the head. We use these distributions in models 1a, 2a and 3a.

In addition, we define a uniform distribution spanning from the minimum to the maximum of the reported values for all the tissue classes and refer to it as the extended distribution (EXT). This uniform distribution is used for all the tissues in models 1b, 2b and 3b. To indicate a known deterministic value of the tissue conductivities, we use the vector $\boldsymbol{\sigma} = [\sigma_1, \sigma_2, \dots, \sigma_d]$, whereas we use $\boldsymbol{\Sigma} = [\Sigma_1, \Sigma_2, \dots, \Sigma_d]$ to refer to the vector containing the random parameters modelled by the distributions.

As explained in section 2.1, we consider three different geometries for the skull going from a single isotropic volume in model 1 to a three shell design where the outer table and inner table are differentiated in model 3. For each geometry i , we consider two sets of conductivity distributions: either those introduced in [11], giving $\boldsymbol{\Sigma}_a = [\Sigma_{\text{WM}}, \Sigma_{\text{GM}}, \dots, \Sigma_{\text{SCP}}]$, or the same extended distribution for each of the tissues, i.e. $\boldsymbol{\Sigma}_b = [\Sigma_{\text{EXT}}, \Sigma_{\text{EXT}}, \dots, \Sigma_{\text{EXT}}]$. So for each geometric model, 1 to 3, we obtain two models, a or b, depending on the conductivity distributions used. The parameters of the distributions as well as the tissues included in each model are shown in Table 1.

2.4 EEG forward problem

When carrying out an EEG source reconstruction analysis, one acquires the evoked potentials induced on the scalp by the underlying brain activity. This electrical activity is generally modelled by one or more electric current dipoles characterised by their coordinates in space $\boldsymbol{r} = [r_x, r_y, r_z]$ and their dipole moment $\boldsymbol{p} = [p_x, p_y, p_z]$ (Am).

To reduce the computational cost, a set of discrete sources is considered rather than the full continuous volume of the gray matter. This set is called a source space and defines potential dipoles locations.

The relation between the source space containing n sources and the electric potential measured on m electrode at the scalp level is given by the expression

$$[l] \cdot \boldsymbol{s} + \boldsymbol{e} = \boldsymbol{v}, \quad (5)$$

where $\boldsymbol{s} = [p_1^{(x)}, p_1^{(y)}, p_1^{(z)}, \dots, p_n^{(x)}, p_n^{(y)}, p_n^{(z)}]^\top$ is the source vector and $p_j^{(k)}$ is the dipole moment of the source located in the j -th site along k -axis, $\boldsymbol{e} = [e_1, \dots, e_m]^\top$ and $\boldsymbol{v} = [v_1, \dots, v_m]^\top$ are respectively the additive noise component vector and the vector of electrodes potentials (V), and $[l]$ is equally referred to as the leadfield or gain matrix.

This matrix looks like this

$$[l] = \begin{bmatrix} l_{1,1}^{(x)} & l_{1,1}^{(y)} & l_{1,1}^{(z)} & \dots & l_{1,n}^{(x)} & l_{1,n}^{(y)} & l_{1,n}^{(z)} \\ \vdots & \vdots & \vdots & \ddots & \vdots & \vdots & \vdots \\ l_{m,1}^{(x)} & l_{m,1}^{(y)} & l_{m,1}^{(z)} & \dots & l_{m,n}^{(x)} & l_{m,n}^{(y)} & l_{m,n}^{(z)} \end{bmatrix}, \quad (6)$$

where each element $l_{i,j}^{(k)}$ corresponds to the electric potential v measured on the i -th electrode due to a current dipole with unitary dipole moment located on the j -th site and oriented along k -axis ($\text{VA}^{-1}\text{m}^{-1}$). This model encompasses all the geometric information and the physical properties. In the rest of this paper, the notation $[l(\boldsymbol{\sigma})]$ is used when highlighting the dependences of the leadfield on the values set for the electrical conductivity.

Here, we compute $[l]$ on an element basis, i.e. in each tetrahedral element of the mesh, following the method described in [22] based on the reciprocity principle: in order to obtain the voltage difference between two points due to a single current dipole, one only need to compute the electric field \boldsymbol{e} at the coordinates of the dipole resulting from the injection of a 1 A current i between the two points.

$$v_1 - v_2 = \frac{\boldsymbol{e} \cdot \boldsymbol{p}}{i} \quad (7)$$

The method then consists in setting a reference electrode and iteratively injecting a 1 A current through the m active electrodes and acquiring the electric field on the source space in the i -th row of the matrix $[l]$.

This step of the process is achieved in *GetDP* with the generalised minimal residual method (GMRES) configured with a tolerance of 10^{-8} and an incomplete factorisation (ILU) preconditioner.

Given that brain activity only occurs in the gray matter, that the mesh for that tissue is made of about 368000 tetrahedra and that we have setup 59 active electrodes, the whole leadfield matrix $[l]_{\text{full}}$ would theoretically have a size of $59 \times (3 \times 368000)$, which is too large for practical use. Therefore we arbitrarily fix the average interval between two sources at 7.5 mm, resulting in 2127 sources and a leadfield matrix $[l] \in \mathbb{R}^{59 \times 6381}$ which is more manageable.

2.5 Sensitivity analysis

As defined in [23], sensitivity analysis is the study of how variation in the input parameters of a process influences the variation in the output. In this field, two cases are differentiated. The local sensitivity focuses on the uncertainty at a specific coordinate of the parameters space Ω whereas the global sensitivity captures the variation across the whole space.

One of the most used and studied global sensitivity analysis techniques is the computation of the so called Sobol indices [24,25]. Let us consider a model $Y = Y(\boldsymbol{X})$ where Y is the random output variable and $\boldsymbol{X} = [X_1, \dots, X_{n_p}]$ is the vector of n_p random input variables. The first and total order Sobol indices for the i -th input variable, s_i and



















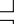

















Name	Tissue		Parameters (Sm ⁻¹)				Model		
	Abbr.	Color	Min.	Max.	Mean	Std.	1	2	3
Scalp	SCP		0.1370	2.1000	0.4137	0.1760			
Skull (Whole)	SKL		0.0182	1.7180	0.0160	0.0190			
Skull (Spongy)	SKL SPG		0.0012	0.2890	0.0497	0.0735			
Skull (Compact)	SKL CPT		0.0024	0.0079	0.0046	0.0016			
Skull (Outer table)	SKL OCPT		0.0008	0.0078	0.0049	0.0029			
Skull (Inner table)	SKL ICPT		0.0028	0.0129	0.0068	0.0036			
Cerebrospinal fluid	CSF		1.0000	2.5100	1.7100	0.2981			
Gray matter	GM		0.0600	2.4700	0.4660	0.2392			
White matter	WM		0.0646	0.8100	0.2167	0.1703			
Extended	EXT	-	0.0008	2.5100	-	-	-	-	-

Table 1: The tissues used in this work with the parameters of the corresponding electrical conductivity distributions from [11]. The last three columns show which tissues are included in each model.

$s_i^{(t)}$ are defined by

$$s_i = \frac{\mathbb{V}_{X_i}(\mathbb{E}_{\mathbf{X}_{\setminus i}}(Y | X_i))}{\mathbb{V}(Y)}, \quad (8)$$

$$s_i^{(t)} = \frac{\mathbb{E}_{\mathbf{X}_{\setminus i}}(\mathbb{V}_{X_i}(Y | \mathbf{X}_{\setminus i}))}{\mathbb{V}(Y)}, \quad (9)$$

where $\mathbf{X}_{\setminus i}$ is the vector of all the random inputs but X_i , s_i corresponds to the variance in the output explained by X_i alone, $\mathbb{V}_{X_i}(\mathbb{E}_{\mathbf{X}_{\setminus i}}(Y | X_i))$ is the variance explained by the i -th parameter, also referred to as its main effect, and $s_i^{(t)}$ is the output variance explained by X_i and all its interactions with the other input parameters.

To compute Sobol indices, we follow the method presented in [25] and implemented in the python package *SALib* [26] that provides a way to compute both s_i and $s_i^{(t)}$ from the same set of evaluations of the model thus reducing the amount of computation required. This technique relies on n_d observations $\{(y_i^{(d)}, \mathbf{x}_i^{(d)}), i = 1, \dots, n_d\}$ where each $y_i^{(d)} = y(\mathbf{x}_i^{(d)})$ is the output of the model for a set of inputs $\mathbf{x}_i^{(d)} = [x_{i,1}^{(d)}, \dots, x_{i,n_p}^{(d)}]$. Let us define $\mathbf{y}^{(d)} = [y_1^{(d)}, \dots, y_{n_d}^{(d)}]^\top$ the vector of outputs and $[\mathbf{x}]^{(d)} = [\mathbf{x}_1^{(d)}, \dots, \mathbf{x}_{n_d}^{(d)}]^\top$ the matrix of inputs.

The matrix $[\mathbf{x}]^{(d)}$ is built of $n_p + 2$ sub-matrices: $[a]$, $[b]$ and the matrices $[a_b]^{(i)}$ where all the columns are the same as in $[a]$ except the i -th one coming from $[b]$. All these matrices have n_r rows and n_p columns. The input vectors $\mathbf{x}_i^{(d)}$ composing the independent matrices $[a]$ and $[b]$ are drawn from the parameters space Ω using the Saltelli extension of Sobol quasi-random sequence [27, 28]. Such sequences are described in section 2.6.

Based on these samples, the numerators of Equations (8) and (9) are computed with

$$\begin{aligned} & \mathbb{V}_{X_i}(\mathbb{E}_{\mathbf{X}_{\setminus i}}(Y | X_i)) \\ &= \frac{1}{n_r} \sum_{j=1}^{n_r} \mathbf{y}([b])_j \left(\mathbf{y}([a_b]^{(i)})_j - \mathbf{y}([a])_j \right), \end{aligned} \quad (10)$$

$$\begin{aligned} & \mathbb{E}_{\mathbf{X}_{\setminus i}}(\mathbb{V}_{X_i}(Y | \mathbf{X}_{\setminus i})) \\ &= \frac{1}{2n_r} \sum_{j=1}^{n_r} \left(\mathbf{y}([a])_j - \mathbf{y}([a_b]^{(i)})_j \right)^2. \end{aligned} \quad (11)$$

2.6 Surrogate model

The computation of the sensitivity indices described in section 2.5 requires a large number of model evaluations. When the actual model (here the computation of the lead-field matrix) is computationally heavy, a simpler model, referred to as the surrogate model, can be used instead. This simpler version must behave almost like if it were the real one but its evaluation should require less computing power.

Building such a model is the goal of all the supervised learning techniques. Those methods start from a set of n_d observations $\mathbf{y}^{(d)} = [y_1^{(d)}, \dots, y_{n_d}^{(d)}]^\top$ of the actual model at different points of the parameters space $[\mathbf{x}]^{(d)} = [\mathbf{x}_1^{(d)}, \dots, \mathbf{x}_{n_d}^{(d)}]^\top$ where $y_i^{(d)} = y(\mathbf{x}_i^{(d)})$ with $y(\mathbf{x})$ the real model. From this relatively small amount of evaluations of the model, the surrogate model $\hat{y}(\mathbf{x})$ is built so that $\hat{y} = \hat{y}(\mathbf{x}) \approx y(\mathbf{x})$ for any vector $\mathbf{x} \in \Omega$ that is not in the training set $[\mathbf{x}]^{(d)}$.

The first step for building the surrogate model is then to draw n_d vectors $\mathbf{x}_i^{(d)}$ to build the matrix $[\mathbf{x}]^{(d)}$. This can be performed with various methods but here we consider quasi-random sequences. Those sequences, compared to real random sequences, take into account the previous points that have been drawn. They are used to cover the space as efficiently as possible. In section 2.5 the Saltelli extension of Sobol sequence is used to define the coordinates and here, to produce the training set for the surrogate model, we use a Halton sequence [29] as implemented in *chaospy* [30].

In *shamo*, the generation of the surrogate model is carried out with "Gaussian Processes Regression" (GPR) [31]. Let us define the notation for a multivariate normal distribution $\mathcal{N}(\boldsymbol{\mu}, [\boldsymbol{\gamma}])$ where $\boldsymbol{\mu} = [\mu_1, \dots, \mu_{n_p}]$ is the vector of means along each axis and $[\boldsymbol{\gamma}]$ is the covariance matrix where each $\gamma_{i,i}$ is the variance of the i -th random parameter and the elements $\gamma_{i,j}$ are the correlation between the i -th and the j -th variables.

To predict the n_t values $\mathbf{y}^{(t)} = [y_1^{(t)}, \dots, y_{n_t}^{(t)}]^\top$ on the test points $[\mathbf{x}]^{(t)}$, GPR handles the problem as Bayesian inference. Under these conditions, the learning samples are treated as random variables following a multivariate normal distribution $P(\mathbf{y}^{(d)} | [\mathbf{x}]^{(d)}) = \mathcal{N}(\boldsymbol{\mu}^{(d)}, [\boldsymbol{\gamma}]^{(d)})$. Here, the mean of this distribution is set to the mean of the learning outputs. To consider the test points, this expres-

sion becomes

$$P(\mathbf{y}^{(d)}, \mathbf{y}^{(t)} | [x]^{(d)}) = \mathcal{N}\left(\mu^{(d)}, \begin{bmatrix} [\gamma]^{(t)} & [\gamma]^{(t,d)} \\ [\gamma]^{(d,t)} & [\gamma]^{(d)} + \epsilon[i] \end{bmatrix}\right), \quad (12)$$

with ϵ an added noise.

Next, the conditional distribution $P(\mathbf{y}^{(t)} | \mathbf{y}^{(d)}, [x]^{(d)}) = \mathcal{N}(\mu^*, [\gamma]^*)$ is obtained with

$$\mu^* = \mu^{(d)} + [\gamma]^{(t,d)}([\gamma]^{(d)})^{-1}(\mathbf{y}^{(d)} - \mu^{(d)}), \quad (13)$$

$$[\gamma]^* = [\gamma]^{(t)} - [\gamma]^{(t,d)}([\gamma]^{(d)})^{-1}[\gamma]^{(d,t)}. \quad (14)$$

Finally, the mean values μ_i^* and the standard deviation $\gamma_i^* = [\gamma]_{i,i}^*$ are obtained by the marginalisation of each random variable. The values μ_i^* are the predictors corresponding to the test points.

During the training step, the hyper-parameters of the kernel are optimised by maximising the log-marginal likelihood (LML) [32]. When the model outputs more than one scalar, the process can be applied separately to each of the outputs, giving one Gaussian process by output variable.

Here, we use the implementation of the GPR from *scikit-learn* [33] and follow the recommendations from [34]. Thus, the regression part of the GPR is set to the mean of the output variable and the kernel is obtained by the product of a constant kernel and a stationary Matérn kernel with the smoothness parameter $\nu = 2.5$, thus resulting in the covariance function

$$k(\mathbf{x}_1, \mathbf{x}_2) = \left(1 + \frac{\sqrt{5}}{l}d(\mathbf{x}_1, \mathbf{x}_2) + \frac{5}{3l}d(\mathbf{x}_1, \mathbf{x}_2)r\right) \cdot \exp\left(-\frac{\sqrt{5}}{l}d(\mathbf{x}_1, \mathbf{x}_2)\right). \quad (15)$$

3 Applications

3.1 EEG forward problem

Now that the methods involved in the pipeline are introduced, we apply it to the computation of the EEG leadfield matrix. As described in section 2.4, the computation of the forward model is of main interest in source reconstruction but is highly dependent on the geometry and the physical properties of the tissues.

To build the surrogate model, we generate a set of leadfield matrices $[l(\boldsymbol{\sigma}^{(i)})]$ for around a hundred conductivity vectors $\boldsymbol{\sigma}^{(i)}$ drawn from the parameters space Ω using a Halton sequence. This step results in a leadfield matrix where each element is actually a Gaussian process, which gives us the ability to quickly construct any new matrix $[l(\boldsymbol{\sigma})]$.

Considering the sensitivity indices defined in Equations (8) and (9) are only valid for a model with a single scalar output, we choose the following metric to study the sensitivity of the whole matrix to the values of $\boldsymbol{\sigma}$

$$m(\boldsymbol{\sigma}) = \|[l(\boldsymbol{\sigma})] - [l]_{\text{ref}}\|_F, \quad (16)$$

with $[l]_{\text{ref}}$ the leadfield matrix obtained when using $\boldsymbol{\sigma} = \boldsymbol{\sigma}_{\text{ref}}$ which, here, is the mean value for each tissue (See Table 1).

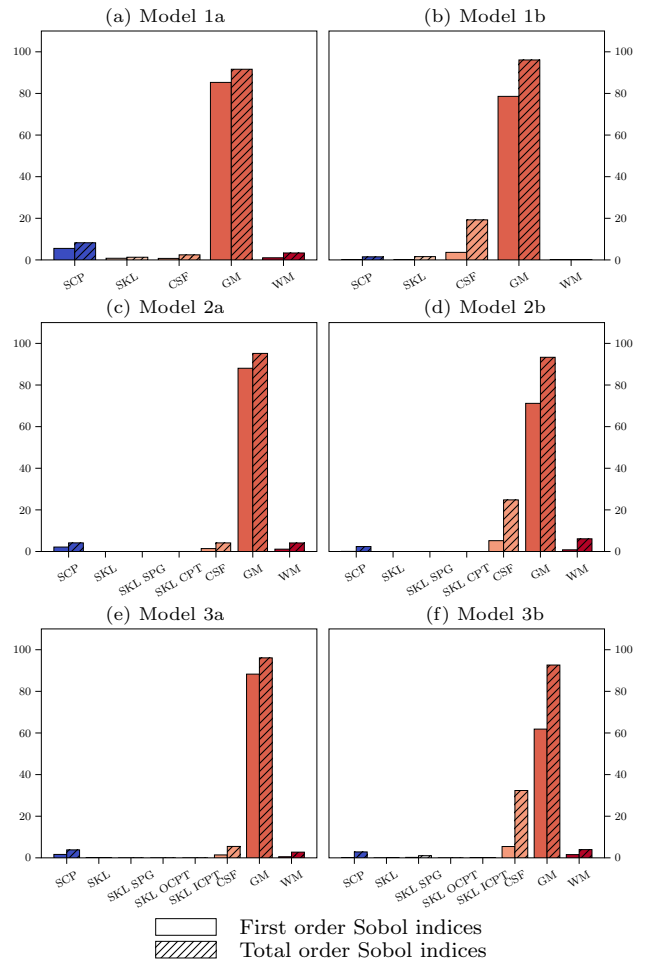


Fig. 2: First and total order Sobol indices of the metric $m(\boldsymbol{\sigma})$ for each tissue of each model. In the left column, the values for $\boldsymbol{\Sigma}$ are the truncated normal distributions from [11] and in the right column, the extended uniform distribution is used.

A surrogate model $\hat{m}(\boldsymbol{\sigma})$ is thus built for this function based on the same training data as the parametric matrix introduced above. Next, the first and total order Sobol indices are computed from two sets of 40000 evaluations of the Gaussian process for the six models of this study. The resulting indices are shown in Figure 2.

Clearly, for both the truncated distributions and the extended uniform one, the parameter with the biggest influence on the metric is the conductivity of the gray matter σ_{GM} . Whether one uses the narrow truncated normal (models 2a/3a) or the extended uniform (models 2b/3b) distributions for the compact skull and the outer and inner tables has little influence on the Sobol indices.

Another point of interest in these results is the rising influence of the CSF when the uniform distribution is used. While both its first and total order Sobol indices in models 1a to 3a are very small, the value of $s_{\text{CSF}}^{(t)}$ for models 1b to 3b are non negligible meaning there are interactions between parameters.

3.2 Evaluation of the electrodes potential

To illustrate the actual effect of the sensitivity described in the above application, we calculate the electrical potential measured on the scalp due to a single left frontal source.

Model 3 with the σ_{ref} was used as a reference (Figure 3b) then the conductivity of GM was also set to the minimal and maximal value found in the literature (See Table 1) and the scalp map difference calculated (Figure 3 c and d).

3.3 Transcranial direct current stimulation (tDCS) simulation

Using the same formulation as for the EEG forward problem, we can model tDCS and obtain the current density, electric potential and electric field across the whole head.

To illustrate this feature, we considered a HD-tDCS experiment where electrode P3 was set as a 4 mA injector and electrodes TP9, C3, P1 and O1 were set to ground. We used the mesh from model 3 and the truncated normal conductivity distributions as in model 3a for this simulation. As a metric, we chose the mean of the norm of the current density in an arbitrary small shallow region of the left parietal lobe. The results of these simulations are shown in Figure 4.

As an extra feature for researchers in neuroscience, the estimated fields can also be directly exported as a standard multidimensional NifTI image.

4 Discussion

The pipeline presented in this work uses several well established methods. Here, we discuss the added value of such tool and the choices of techniques.

First, the generation of a realistic subject specific head model is generally a tedious work. It requires to accurately segment the head volume based on MRI or CT acquired images. Next, one must compute the surfaces at the interfaces of the tissues. This step often requires further cleaning to ensure the surfaces are two dimensional manifold, which, simply put, means they are completely closed and thus have an inside and an outside. Then, those surfaces must be integrated into a single mesh and the so defined volumes filled with tetrahedral elements. Here the FEM mesh is directly built from a 3D image made of labelled voxels. This technique not only provides more control on the refinement of the final mesh but also makes it easier to include more tissues with complex geometries. Moreover, this opens the path for more specific cases such as modelling prosthetic, metallic plates or any other unusual head geometry.

As explained previously, the model presented in this paper does not consider the anisotropy of white matter because no tensor information is provided with the MIDA model. However any kind of field can be included in the model and handled by the tool. Since the solving part is fully achieved in *GetDP*, adding such fields does not induce any additional work from the point of view of the user.

In addition, the usage of *GetDP* allows us to add any simulation based problem. The tool can thus be extended to allow the computation of any field occurring in the head with respect to some experimental parameters. The electrical conductivity is not the only parameter that can be

studied. The injected current for the HD-tDCS is an example.

In fact, the addition of a new application field such as MEG or tMS only requires the definition of the equations related to the problem, which are explicitly stored in a problem file in *GetDP* and to derive the python classes available in *shamo* to expose the needed parameters. This flexible implementation allows the user to define his own processes.

We decided to use Gaussian process as surrogate models because they provide information on the confidence over the solution through the standard deviation on each predicted point. This can be used to get a more in-depth understanding of the model. This kind of regressors also has the advantage of not requiring a very large amount of training data. Considering the fact that an evaluation of the actual model can take several hours, reducing the number of observations can drastically lower the computation time required.

To further reduce this time, the tool provides an easy way to evaluate each point separately, thus allowing the user to use high-performance computing (HPC) equipment like computer clusters. In the present work, observations were computed by batches of 100, each on a single core on the clusters of the CECI.

Another import point to discuss is the sensitivity indices used. Since the definition of the Sobol indices rely on a single scalar output function, the choice of the metric is important. Thus, it depends on the effect the user tries to show.

Finally, one might wonder what is the difference between *shamo* and, for instance, a software like SimNIBS [35]. First, while SimNIBS is dedicated to brain stimulation, our package can easily be extended to many other simulations. Moreover, the finite element generation is as simple as it can get and does not solely rely on pre-computed surfaces. Finally, the goal of *shamo* is to provide a single tool to go from FEM creation to sensitivity analysis with few dependencies that are all open source and work out of the box on any major operating system or on HPC.

5 Conclusion

In this paper, we presented a python pipeline for accurate electromagnetic modelling of the head which allows for sensitivity analysis and surrogate model building. This tool, called *shamo* [9], and the full documentation [36] are available on Github under GPL-v3 license. A set of examples are also available in the form of jupyter notebooks.

We showed a use-case for the EEG forward problem where a parametric leadfield matrix is computed and can then be used to generate any new matrix for a specific set of σ and another application to tDCS where the current density in a certain region is obtained and can be studied with regard to the electrical sensitivity. Those are only two possible applications but *shamo* could easily be extended to magnetic stimulation or tMS.

Considering the abstraction level of the tool and the outcome that can be obtained from it, one can use our tool

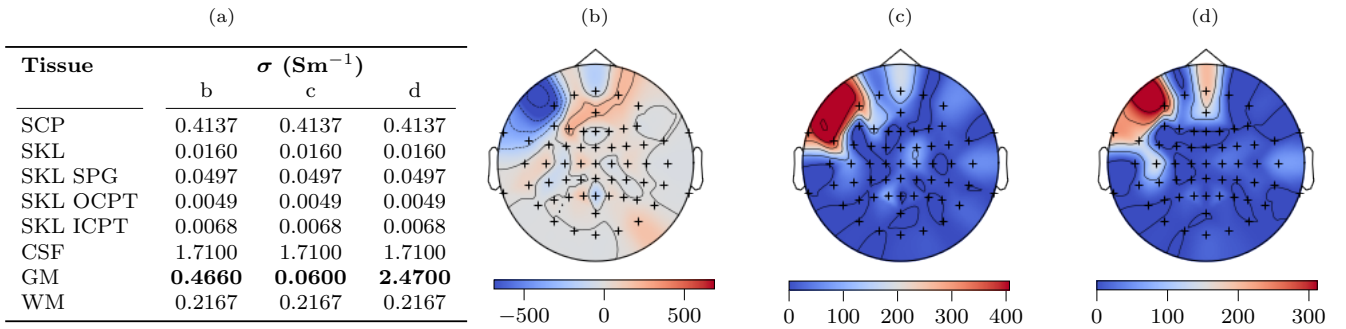


Fig. 3: (a) The values of σ used for the three other figures, (b) the scalp potential $v(\sigma_{\text{ref}})$ (mV) computed for $\sigma_b = \sigma_{\text{ref}}$, (c) and (d) the absolute difference between the reference scalp potential and the potential computed for the two other $|v(\sigma) - v(\sigma_{\text{ref}})|$ (mV).

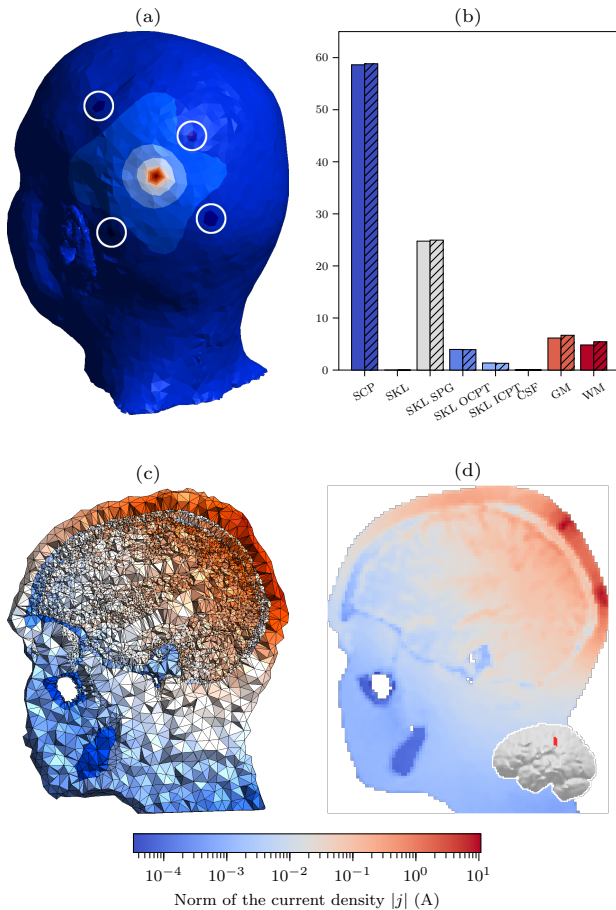


Fig. 4: (a) A view of the scalp potential induced by the set electrodes surrounded in white, (b) the first and total order Sobol indices of the mean current density in the ROI for each tissue conductivity, (c) a cut of the current density inside the head resulting from the injection of current inside the reference model where $\sigma = \sigma_{\text{ref}}$ and (d) the same information in the form of a NIFTI file with a representation of the small mask used to compute the mean of the norm of the current density.

to perform finite element analysis and sensitivity analysis without having to dig into those fields, letting the user employ the toolset of his choice for further analysis. *shamo* could be used in many studies to assess the sensitivity of the results to some parameters or to build parametric models for complex physical fields that, otherwise, should be evaluated every time a new value is needed.

Acknowledgements

Computational resources have been provided by the Consortium des Équipements de Calcul Intensif (CÉCI), funded by the Fonds de la Recherche Scientifique de Belgique (F.R.S.-FNRS) under Grant No. 2.5020.11 and by the Walloon Region.

References

- [1] D. S. Tuch, V. J. Wedeen, A. M. Dale, J. S. George, and J. W. Belliveau, “Conductivity tensor mapping of the human brain using diffusion tensor MRI,” *Proceedings of the National Academy of Sciences*, vol. 98, pp. 11697–11701, Sept. 2001.
- [2] J. Haueisen, C. Ramon, P. Czapski, and M. Eiselt, “On the influence of volume currents and extended sources on neuromagnetic fields: A simulation study,” *Annals of Biomedical Engineering*, vol. 23, pp. 728–739, Nov. 1995.
- [3] J. Haueisen, C. Ramon, M. Eiselt, H. Brauer, and H. Nowak, “Influence of tissue resistivities on neuromagnetic fields and electric potentials studied with a finite element model of the head,” *IEEE Transactions on Biomedical Engineering*, vol. 44, pp. 727–735, Aug. 1997.
- [4] J. Haueisen, D. Tuch, C. Ramon, P. Schimpf, V. Wedeen, J. George, and J. Belliveau, “The Influence of Brain Tissue Anisotropy on Human EEG and MEG,” *NeuroImage*, vol. 15, pp. 159–166, Jan. 2002.
- [5] R. J. Sadleir and A. Argibay, “Modeling Skull Electrical Properties,” *Annals of Biomedical Engineering*, vol. 35, pp. 1699–1712, Sept. 2007.
- [6] M. Dannhauer, B. Lanfer, C. H. Wolters, and T. R. Knösche, “Modeling of the human skull in EEG source analysis,” *Human Brain Mapping*, vol. 32, pp. 1383–1399, Sept. 2011.
- [7] M. R. Bashar, Y. Li, and P. Wen, “Uncertainty and sensitivity analysis for anisotropic inhomogeneous head tissue conductivity in human head modelling,” *Australasian Physical & Engineering Sciences in Medicine*, vol. 33, pp. 145–152, June 2010.
- [8] Z. Wu, Y. Liu, M. Hong, and X. Yu, “A review of anisotropic conductivity models of brain white matter based on diffusion tensor imaging,” *Medical & Biological Engineering & Computing*, vol. 56, pp. 1325–1332, Aug. 2018.

- [9] M. Grignard, “shamo.” <https://doi.org/10.5281/zenodo.4420811>, Jan. 2021.
- [10] M. I. Iacono, E. Neufeld, E. Akinagbe, K. Bower, J. Wolf, I. Vogiatzis Oikonomidis, D. Sharma, B. Lloyd, B. J. Wilm, M. Wyss, K. P. Pruessmann, A. Jakab, N. Makris, E. D. Cohen, N. Kuster, W. Kainz, and L. M. Angelone, “MIDA: A Multimodal Imaging-Based Detailed Anatomical Model of the Human Head and Neck,” *PLOS ONE*, vol. 10, p. e0124126, Apr. 2015.
- [11] H. McCann, G. Pisano, and L. Beltrachini, “Variation in Reported Human Head Tissue Electrical Conductivity Values,” *Brain Topography*, vol. 32, pp. 825–858, Sept. 2019.
- [12] H. Hallez, B. Vanrumste, R. Grech, J. Muscat, W. De Clercq, A. Vergult, Y. D’Asseler, K. P. Camilleri, S. G. Fabri, S. Van Huffel, and I. Lemahieu, “Review on solving the forward problem in EEG source analysis,” *Journal of NeuroEngineering and Rehabilitation*, vol. 4, p. 46, Dec. 2007.
- [13] E. Ziegler, S. L. Chellappa, G. Gaggioni, J. Q. Ly, G. Vandewalle, E. André, C. Geuzaine, and C. Phillips, “A finite-element reciprocity solution for EEG forward modeling with realistic individual head models,” *NeuroImage*, vol. 103, pp. 542–551, Dec. 2014.
- [14] T. C. Project, *CGAL User and Reference Manual*. CGAL Editorial Board, 5.0.3 ed., 2020.
- [15] C. Geuzaine and J.-F. Remacle, “Gmsh: a three-dimensional finite element mesh generator with built-in pre- and post-processing facilities,” *International Journal for Numerical Methods in Engineering*, vol. 79, no. 11, pp. 1309–1331, 2009.
- [16] M. R. Nuwer, “10-10 electrode system for EEG recording,” *Clinical Neurophysiology*, vol. 129, p. 1103, May 2018.
- [17] R. Plonsey and D. B. Heppner, “Considerations of quasi-stationarity in electrophysiological systems,” *The Bulletin of Mathematical Biophysics*, vol. 29, pp. 657–664, Dec. 1967.
- [18] J. Malmivuo and R. Plonsey, *Bioelectromagnetism: Principles and Applications of Bioelectric and Biomagnetic Fields*. Oxford University Press, Oct. 1995.
- [19] P. H. Schimpf, “Application of Quasi-Static Magnetic Reciprocity to Finite Element Models of the MEG Lead-Field,” *IEEE Transactions on Biomedical Engineering*, vol. 54, pp. 2082–2088, Nov. 2007. Conference Name: IEEE Transactions on Biomedical Engineering.
- [20] D. Güllmar, J. Haueisen, and J. R. Reichenbach, “Influence of anisotropic electrical conductivity in white matter tissue on the EEG/MEG forward and inverse solution. A high-resolution whole head simulation study,” *NeuroImage*, vol. 51, pp. 145–163, May 2010.
- [21] C. Geuzaine, “GetDP: a general finite-element solver for the de Rham complex,” *PAMM Volume 7 Issue 1. Special Issue: Sixth International Congress on Industrial Applied Mathematics (ICIAM07) and GAMM Annual Meeting, Zürich 2007*, vol. 7, no. 1, pp. 1010603–1010604, 2007.
- [22] D. Weinstein, L. Zhukov, and C. Johnson, “Lead Field Basis for FEM Source Localization,” *Annals of Biomedical Engineering*, vol. 28, no. 9, pp. 1059–1065, 2000.
- [23] A. Saltelli, ed., *Global sensitivity analysis: the primer*. Chichester, England ; Hoboken, NJ: John Wiley, 2008. OCLC: ocn180852094.
- [24] I. Sobol’, “Global sensitivity indices for nonlinear mathematical models and their Monte Carlo estimates,” *Mathematics and Computers in Simulation*, vol. 55, pp. 271–280, Feb. 2001.
- [25] A. Saltelli, P. Annoni, I. Azzini, F. Campolongo, M. Ratto, and S. Tarantola, “Variance based sensitivity analysis of model output. Design and estimator for the total sensitivity index,” *Computer Physics Communications*, vol. 181, pp. 259–270, Feb. 2010.
- [26] J. Herman and W. Usher, “SALib: An open-source Python library for Sensitivity Analysis,” *Journal of Open Source Software*, vol. 2, p. 97, Jan. 2017.
- [27] I. Sobol’, “On the distribution of points in a cube and the approximate evaluation of integrals,” *USSR Computational Mathematics and Mathematical Physics*, vol. 7, pp. 86–112, Jan. 1967.
- [28] I. Sobol’, “Uniformly distributed sequences with an additional uniform property,” *USSR Computational Mathematics and Mathematical Physics*, vol. 16, pp. 236–242, Jan. 1976.
- [29] J. H. Halton, “On the efficiency of certain quasi-random sequences of points in evaluating multi-dimensional integrals,” *Numerische Mathematik*, vol. 2, pp. 84–90, Dec. 1960.
- [30] J. Feinberg and H. P. Langtangen, “Chaospy: An open source tool for designing methods of uncertainty quantification,” *Journal of Computational Science*, vol. 11, pp. 46–57, Nov. 2015.
- [31] C. E. Rasmussen and C. K. I. Williams, *Gaussian processes for machine learning*. Adaptive computation and machine learning, Cambridge, Mass: MIT Press, 2006. OCLC: ocm61285753.
- [32] A. Schirru, S. Pampuri, G. De Nicolao, and S. McLoone, “Efficient Marginal Likelihood Computation for Gaussian Process Regression,” *arXiv:1110.6546 [stat]*, Oct. 2011. arXiv: 1110.6546.
- [33] F. Pedregosa, G. Varoquaux, A. Gramfort, V. Michel, B. Thirion, O. Grisel, M. Blondel, P. Prettenhofer, R. Weiss, V. Dubourg, J. Vanderplas, A. Passos, D. Cournapeau, M. Brucher, M. Perrot, and E. Duchesnay, “Scikit-learn: Machine learning in Python,” *Journal of Machine Learning Research*, vol. 12, pp. 2825–2830, 2011.
- [34] H. Chen, J. L. Loeppky, J. Sacks, and W. J. Welch, “Analysis Methods for Computer Experiments: How to Assess and What Counts?,” *Statistical Science*, vol. 31, pp. 40–60, Feb. 2016.
- [35] A. Thielscher, A. Antunes, and G. B. Saturnino, “Field modeling for transcranial magnetic stimulation: A useful tool to understand the physiological effects of TMS?,” in *2015 37th Annual International Conference of the IEEE Engineering in Medicine and Biology Society (EMBC)*, (Milan), pp. 222–225, IEEE, Aug. 2015.
- [36] M. Grignard, “shamo documentation.” <https://cyclotronresearchcentre.github.io/shamo/index.html>, Jan. 2021.